

## Gates joint locally connected network for accurate and robust reconstruction in optical molecular tomography

Minghua Zhao , Yahui Xiao , Jiaqi Zhang , Xin Cao † and Lin Wang \*,<sup>†</sup>

\**School of Computer Science and Engineering  
Xi'an University of Technology  
Xi'an, China*

<sup>†</sup>*School of Information Science and Technology  
Northwest University, Xi'an 710127, China  
wanglin004@xaut.edu.cn*

Received 11 August 2023

Revised 16 September 2023

Accepted 27 September 2023

Published 4 November 2023

Optical molecular tomography (OMT) is a potential pre-clinical molecular imaging technique with applications in a variety of biomedical areas, which can provide non-invasive quantitative three-dimensional (3D) information regarding tumor distribution in living animals. The construction of optical transmission models and the application of reconstruction algorithms in traditional model-based reconstruction processes have affected the reconstruction results, resulting in problems such as low accuracy, poor robustness, and long-time consumption. Here, a gates joint locally connected network (GLCN) method is proposed by establishing the mapping relationship between the inside source distribution and the photon density on surface directly, thus avoiding the extra time consumption caused by iteration and the reconstruction errors caused by model inaccuracy. Moreover, gates module was composed of the concatenation and multiplication operators of three different gates. It was embedded into the network aiming at remembering input surface photon density over a period and allowing the network to capture neurons connected to the true source selectively by controlling three different gates. To evaluate the performance of the proposed method, numerical simulations were conducted, whose results demonstrated good performance in terms of reconstruction positioning accuracy and robustness.

**Keywords:** Optical molecular tomography; gates module; positioning accuracy; robustness.

### 1. Introduction

Optical molecular imaging (OMI) is an imaging technology that collects the distribution and intensity of light flux on the surface of living organisms, which comes from optical molecular probes

within the organisms.<sup>1</sup> OMI has been widely used in pre-clinical research due to its simplicity, high sensitivity, and noninvasive implementation.<sup>2–4</sup> However, it exists an obvious bottleneck that OMI cannot

This is an Open Access article. It is distributed under the terms of the Creative Commons Attribution 4.0 (CC-BY) License. Further distribution of this work is permitted, provided the original work is properly cited.

quantify the three-dimensional (3D) distribution of the optical signals in imaging objects. Thus, to overcome these limitations, optical molecular tomography (OMT) was further developed. OMT has completed a transformation from two-dimensional (2D) qualitative analysis to 3D quantitative analysis. By fusing structural information of organisms, quantitative distribution of optical probes within the organism can be provided.<sup>5–7</sup> Due to the sparsity of light distribution and the high heterogeneity of biological tissues, imaging accuracy has always been a challenge.<sup>8–10</sup>

To address the issues existing in 3D imaging methods, model-based methods mainly improve from two aspects. On the one hand, by improving the accuracy and efficiency of the optical transmission model, the problem of biological tissue heterogeneity can be solved, which improves the reconstruction results. For example, models such as diffusion approximation, simplified spherical harmonic approximation, and hybrid model are used for OMT.<sup>11–14</sup> On the other hand, strategies such as adding regularization constraints, allowing source regions and multispectral measurements are used for reconstruction, to overcome the ill-posed problem caused by insufficient measurement data and high dimensionality of the model through iterative algorithms and increasing data volume.<sup>15,16</sup> Although these strategies have improved reconstruction performance and achieved accurate and efficient 3D reconstruction, there are still some errors in the approximate optical transmission model compared to the actual optical transmission process, which will be introduced into the final reconstruction results. Model-based methods depend on iterative calculations to solve inverse problems, which is time-consuming. In addition, the accuracy and density of discretized mesh also affect the reconstruction accuracy and resolution seriously.

In recent years, the development of deep learning has provided a new approach for optical 3D reconstruction. Due to its ability to abandon the construction of imaging models and system equations based on mathematical equations, it greatly reduces the pathological nature of 3D reconstruction mathematically and has been successfully applied in the field of OMT.<sup>17–20</sup> Zhang *et al.* proposed a method for CLT reconstruction using multi-layer fully connected neural networks (MFCNNs),<sup>21</sup> and experiments showed that this method has better accuracy and

stability compared to incomplete variables truncated conjugate gradient method. Guo *et al.* proposed an end-to-end 3D depth encoder-decoder network,<sup>22</sup> which greatly improves image quality and significantly reduces reconstruction time. Li *et al.* proposed a deep convolutional framework based on the ResNet architecture for *in vivo* fluorescence reconstruction,<sup>23</sup> achieving high-quality image reconstruction with fewer parameters and relatively high speed. Meng *et al.* developed a K-nearest neighbor-based locally connected (KNN-LC) network to reconstruct the distribution of fluorescence targets in fluorescence molecular tomography,<sup>24</sup> which achieved accurate reconstruction in a short period of time. Moreover, 15% Gaussian noise was added to the KNN-LC network and an accurate source localization with noise interference was achieved. Cao *et al.* proposed an excitation-based fully connected network (EFCN) for the second near-infrared fluorescence molecular tomography with the excitation module and center of barycenter error added to the network and the loss function to improve the positioning accuracy of the light source.<sup>25</sup> Furthermore, 10% Gaussian noise was added to test the robustness of EFCN. The results demonstrated that EFCN improved the quality of FMT reconstruction. However, these reconstruction methods based on deep learning generally lack robustness verification, and their noise resistance needs to be further strengthened. Therefore, 3D imaging methods still need to be further strengthened in terms of network efficiency, reconstruction accuracy, and robustness.

In this paper, inspired by long short-term memory network,<sup>26</sup> which is used to deal with a series of sequence data and allows the network to remember inputs over a period of time, a gates joint locally connected network (GLCN) was proposed. GLCN is composed of a locally connected (LC) network with gate modules embedded aiming to achieve higher accuracy and robustness of OMT reconstruction. The gates module can control different weights for each neuron, enabling the network to selectively capture neurons connected to the true source. To evaluate the performance of GLCN, numerical simulation experiments were conducted. The IVTCG and MFCNN methods were adopted as the baseline for comparisons. The reconstruction results showed that GLCN outperformed in terms of localization accuracy and robustness.

## 2. Materials and Methods

### 2.1. GLCN network architecture

Inspired by long short-term memory network, we tried to use a similar backbone to achieve OMT reconstruction. The whole GLCN architecture is composed of a gate layer with three gate units, a hidden layer and three LC layers (Fig. 1(a)). The number of neurons in the hidden layer and three LC layers is 256, 128, 64, and 3, respectively. The gates module can control and capture the input and output of network information flow by three different gate units (Fig. 1(b)). Compared with the standard fully connected network, the LC layer has the advantage of reducing the quantity of parameter computation. The different network layers of GLCN are partially connected by the dashed line to achieve the neuron information transfer, and this dimensionality reduction operation facilitates GLCN to obtain more accurate results. The surface photon energy  $\Phi$  was obtained by CCD and fed into the network as the input, and the output is the distribution of reconstruction source  $X$ . The whole GLCN-based OMT reconstruction framework is as follows:

$$X = f(\Phi), \quad (1)$$

where  $f$  represents GLCN model, which represents the nonlinear relationship between the surface energy distribution and the light source.  $\Phi$  represents the surface measurements with a dimension of  $n \times 1$ , and  $n$  is the number of nodes in a discrete organism. Further, the inverse problem can be

defined as follows:

$$\min \|f_\theta(y|\theta)\|_2^2, \quad (2)$$

where  $f_\theta$  is the result of the reconstruction network with parameters vector  $\theta$ .  $y$  represents the ground-truth distribution information. The weight  $\theta$  is iteratively updated by minimizing the loss between  $y$  and  $f$ .

The structure of gates module can be calculated as follows:

$$\text{Gate1}_{\text{out}} = \sigma(W(\text{Gate}_{\text{in}})), \quad (3)$$

$$\text{Gate2}_{\text{out}} = \text{Gate1}_{\text{out}} + \delta(\sigma(W(\text{Gate}_{\text{in}}))), \quad (4)$$

$$\text{Gate3}_{\text{out}} = \sigma(W(\text{Gate}_{\text{in}})), \quad (5)$$

$$\text{Gate}_{\text{out}} = \text{Gate3}_{\text{out}}(\delta(\text{Gate2}_{\text{out}})), \quad (6)$$

where  $\text{Gate}_{\text{in}}$  and  $\text{Gate}_{\text{out}}$  denote the input and output of gate layer, respectively;  $\text{Gate1}_{\text{out}}$ ,  $\text{Gate2}_{\text{out}}$ , and  $\text{Gate3}_{\text{out}}$  represent the output of the first, second, and third gate units, respectively;  $W$  refers to network weights;  $\sigma$ ,  $\delta$  are sigmoid, and tanh activation, respectively.

### 2.2. Dataset collection

Considering that deep learning networks are data-driven methods, accumulating ample training samples is necessary. However, directly acquiring the actual distribution of source and the surface photon measurements *in vivo* experiments is unpractical. In this study, we adopted the Monte Carlo (MC) method to generate the simulation

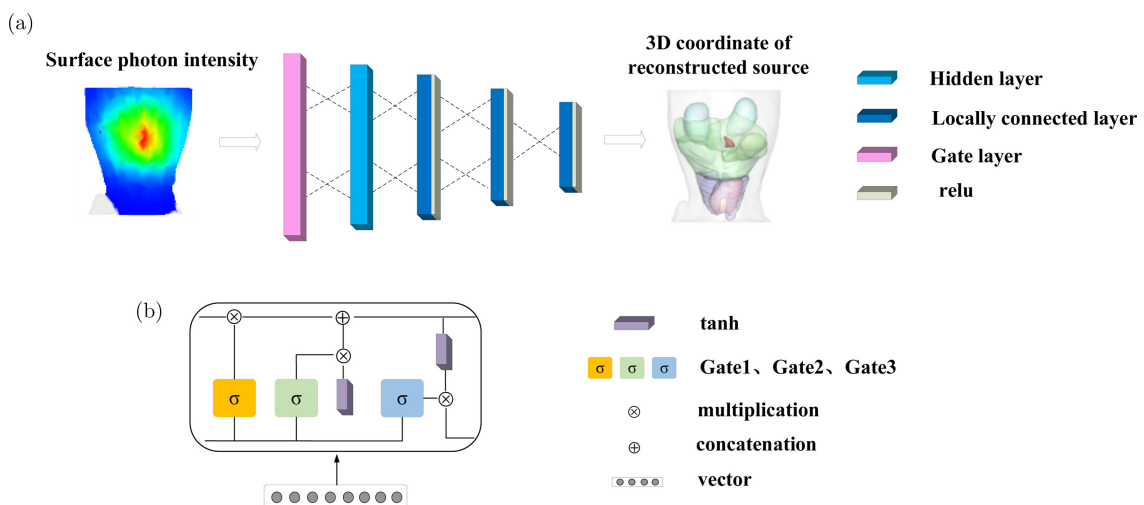


Fig. 1. Schematic illustration of GLCN architecture. (a) The general flow chart of GLCN for OMT reconstruction. (b) Structure of gates module.

samples.<sup>27,28</sup> MC method can provide both surface photon measurements and standard of the actual distribution of the source. In addition, all datasets used in this paper are collected using standard grids discretization from the numerical cylinder model (4626 nodes and 25,840 tetrahedrons) and the numerical mouse model (13,092 nodes and 67,612 tetrahedrons).

In the numerical experiments, this paper generates samples by randomly setting spherical source targets with the radius of 1 mm. For numerical cylinder experiments, 1190 single source samples were produced by the Molecular Optical Simulation Environment (MOSE v2.3)<sup>28</sup> with 190 samples for test set randomly. Meanwhile, 960 single source samples were produced for numerical mouse experiments, in which 96 random samples were used as the test set.

As for the dual-source simulation experiments, data augmentation method was adopted. The dual sources samples were produced by randomly choosing and adding two corresponding single source samples. The data augmentation method can be calculated as follows:

$$\Phi_{d_s} = \sum_{i \in S} \Phi_i, \quad (7)$$

$$X_{d_s} = \sum_{i \in S} X_i, \quad (8)$$

where  $\Phi_{d_s}$ ,  $X_{d_s}$  represent the surface photon energy and the inside source of dual sources assembled, respectively.  $\Phi_i$  means the surface photon of the  $i$ th single source.  $X_i$  refers the  $i$ th single source.  $S$  is the set of selected single-source samples.

Finally, 8820 dual-source samples were collected for the numerical cylinder experiments. During the experiment, 1470 samples were selected randomly for the test set, while the rest of 7350 samples were collected as training set to generate GLCN. Similarly, 8144 dual-source samples were produced for the numerical mouse experiments with 880 dual-source samples chosen for test set.

### 2.3. Network implementation details and evaluation index

All experiments in this paper were accomplished on a computer equipped with an RTX 3080 Ti GPU and a 3.2 GHz Intel Core i9 CPU. The training and testing of deep learning networks are implemented

by Pytorch and Python 3.7. The mean square error (MSE)<sup>29</sup> was adopted as the loss function considering that spatial location is of great significance for OMT reconstruction and directly affects the pre-clinical application.

$$L_{\text{mse}} = \frac{1}{n} \sum (\hat{y}_i - y_i)^2, \quad (9)$$

where  $\hat{y}_i$  and  $y_i$  represent the network's prediction and the ground-truth label of  $i$ th dataset sample, respectively;  $n$  represents the set of elements of  $i$ th dataset sample. Besides, Adam algorithm<sup>30</sup> (learning rate = 0.001,  $\beta_1$ :0.9,  $\beta_2$ :0.99) was adopted as the optimization function of GLCN.

The position error (PE) evaluation index was used in the experiments to measure the reconstruction performance. PE means the position error, which is calculated as the Euclidean distance between the reconstructed source and the ground-truth:

$$\text{PE} = \|\text{ED}(X_r) - \text{ED}(X_t)\|, \quad (10)$$

where  $X_r$  and  $X_t$  means the coordinates of the reconstructed and true sources, respectively. The smaller PE means the more accurate reconstruction result.

## 3. Results

In this section, numerical emulation experiments were used to evaluate the performance of GLCN. IVTCG and MFCNN were used as comparisons. Firstly, numerical simulation experiments were conducted on single and dual light source cylinders. In addition, the results of GLCN in digital mouse simulations were presented, the experiments were also divided into single and dual source experiments. Finally, we listed the reconstruction time of these methods in single source simulation experiments to compare the reconstruction efficiency.

### 3.1. Single-source reconstruction on numerical cylinder simulation

A representative sample has its axis length along  $z$ -axes as 12 mm, where the light source is located. Figure 2(a) shows the 3D view and 2D section images (slice at  $z = 12$  mm) of the reconstructed source using three methods. From the reconstructed result, the IVTCG reconstructed result is oversparse and GLCN is smoother relatively. The result

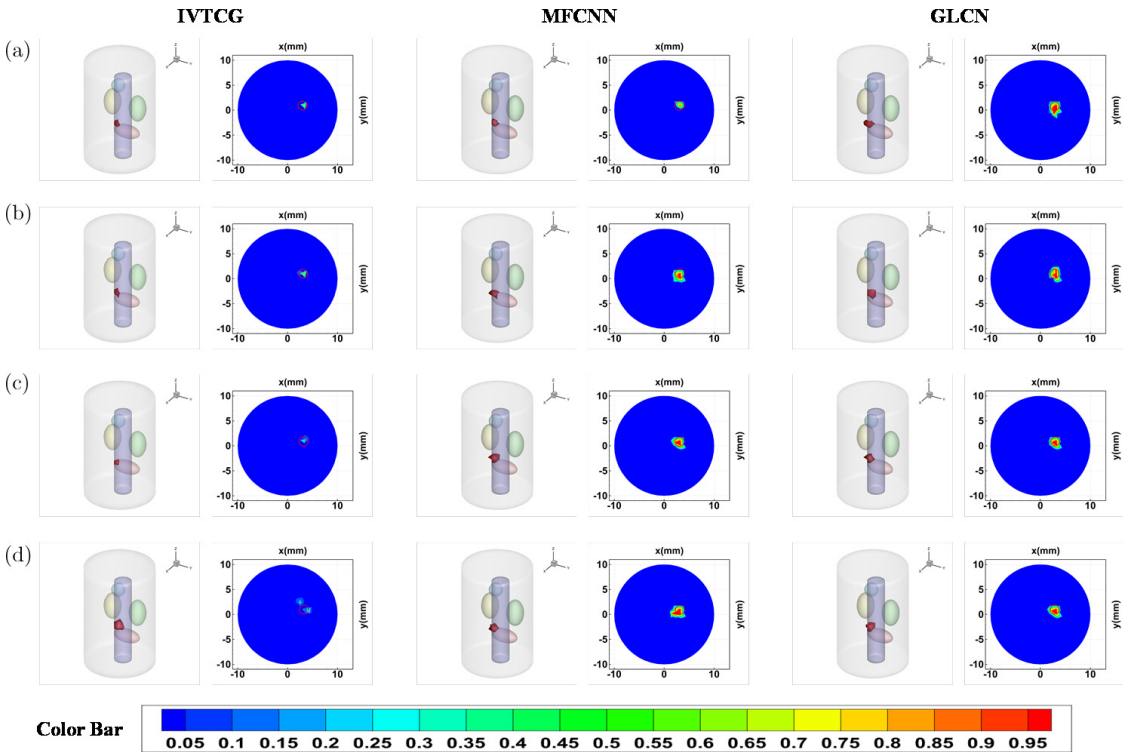


Fig. 2. OMT reconstruction results of single sources with different levels of noise interference using different methods. (a) Displays the 3D view and transverse sections of the reconstructed sources given by IVTCG, MFCNN, and GLCN, respectively. (b)–(d) Depict the 3D view and transverse sections of reconstructed sources with 30%, 60%, 90% Gaussian noise given by IVTCG, MFCNN, and GLCN, respectively. The red cycle represents the true source region.

of MFCNN has significant overlap with the distribution of real light source.

To evaluate the anti-noise ability of the proposed method, different levels (30%, 60%, 90%) of Gaussian noise were added to the measurement data in simulation experiments with test single samples. As displayed in Figs. 2(b)–2(d), the results of the three methods all show changes with noise interference. IVTCG appears blur and divergence.

While MFCNN and GLCN gain distinct results. Compared with MFCNN, GLCN is closer to the true source.

Besides, the quantitative results (mean and standard deviation (SD)) of the three methods are demonstrated in Fig. 3. As shown, GLCN achieves better reconstruction performance with a PE down to  $0.36 \pm 0.18$  mm. With the noise level ranging from 0% to 30%, the PE of IVTCG, MFCNN and GLCN increased by 21.1%, 11.1%, 5.6%, respectively. When the noise level is added to 60% and 90%, the PE of the three methods shows significant changes. However, GLCN still has the minimum PE, which is  $0.51 \pm 0.19$  and  $0.78 \pm 0.28$ , respectively. The results indicate that GLCN possesses superior performance in terms of localization accuracy and anti-noise interference.

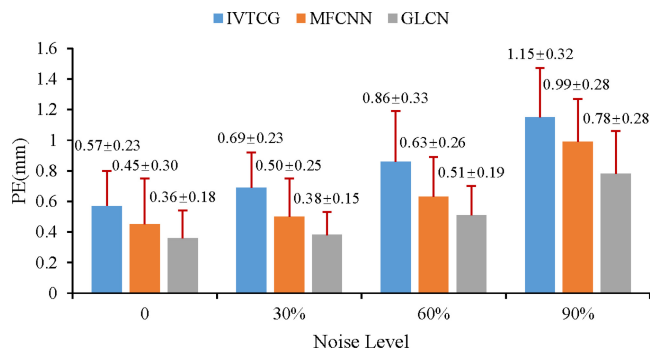


Fig. 3. Quantitative results including the mean and SD of single-source reconstruction with 0, 30%, 60%, 90% Gaussian noise given by IVTCG, MFCNN, and GLCN, respectively.

### 3.2. Dual-source reconstruction on numerical cylinder simulation

The localization accuracy of GLCN is further examined by reconstructing dual-source samples on numerical cylinder simulations. Three dual-source

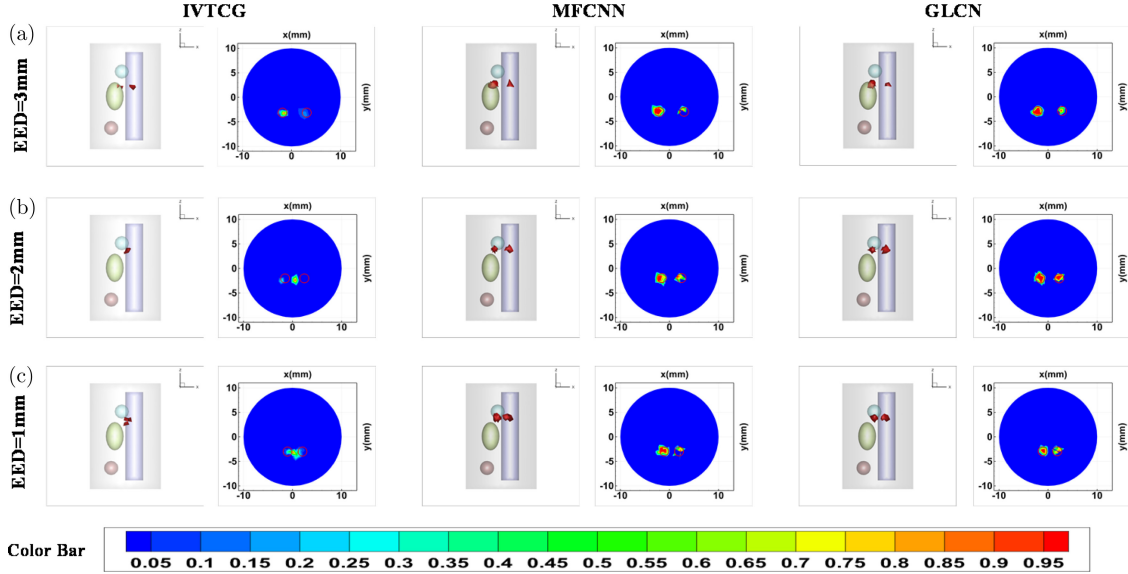


Fig. 4. OMT reconstruction results of dual-source with different EEDs. (a)–(c) demonstrate the reconstructed dual-source using different methods when EEDs are 3 mm, 2 mm, and 1 mm, respectively. Both 3D rendering and 2D transverse sections are depicted for comparisons. The red cycle represents the true source region.

samples with different edge-to-edge distances (EEDs) were reconstructed for display. Their axis length along  $z$ -axes is 18 mm, 20 mm, 20 mm, respectively. Figure 4 displays the 2D transverse sections (taken from  $z = 18$  mm, 20 mm, 20 mm separately) and the 3D reconstruction effects using three different methods. It can be seen from Fig. 4 that when the EED is 3 mm, the result of IVTCG shows an artifact. At this point, MFCNN and GLCN can obtain clearer reconstruction results. When the EED is 2 mm, IVTCG could not correctly reconstruct the light sources. In this case, although both MFCNN and GLCN could distinguish the light sources, one of the reconstruction sources of MFCNN is not significant. When the EED is as small as 1 mm, IVTCG cannot recognize these two light sources, and compared to MFCNN, GLCN is closer to the real source region.

Furthermore, the quantitative error comparison (Fig. 5) shows that the average PE of GLCN compared to EFCN and IVTCG is 33.3–57.8% and 10.7–21.8%, respectively. As the EEDs decrease, the average PE of all three methods increases by varying degrees. As shown in Fig. 5, the error of IVTCG is the highest. However, GLCN gets the lowest average PE of 0.12 mm, 0.16 mm, and 0.26 mm, which indicates that the GLCN provides higher accuracy to reconstruct dual-source. Moreover, the PE value of reconstructed sources S1 and S2 by IVTCG has an obvious difference. While the PE value of reconstructed

sources S1 and S2 by MFCNN and GLCN approaches much relatively. These results all proved the superiority of GLCN in the reconstruction of dual-source.

### 3.3. Single-source reconstruction on digital mouse simulation

For a representative sample with a  $z$ -axis of 13.5 mm, Fig. 6(a) shows the 3D view and 2D section images (slice at  $z = 13.5$  mm) of reconstructed source by three methods. The result of MFCNN is closer to the true source and the second is GLCN, then IVTCG.

Furthermore, 30%, 60%, and 90% Gaussian noise were added to the surface photon density of the single-source sample to test the robustness of GLCN (Figs. 6(b)–6(d)). Under 30% Gaussian noise, the reconstructed results of the three methods remained the same as those without noise in display. With the 60% Gaussian noise, the result of IVTCG appeared artifact. MFCNN and GLCN still could correctly reconstruct the sources. When Gaussian noise is added to 90% level, the experimental results show that only GLCN successfully reconstructs the light source, while the other two methods have poor reconstruction results. These results demonstrate that GLCN has significant advantages in resisting noise interference.

In order to quantitatively compare the performance of reconstruction results, Fig. 7 displays the

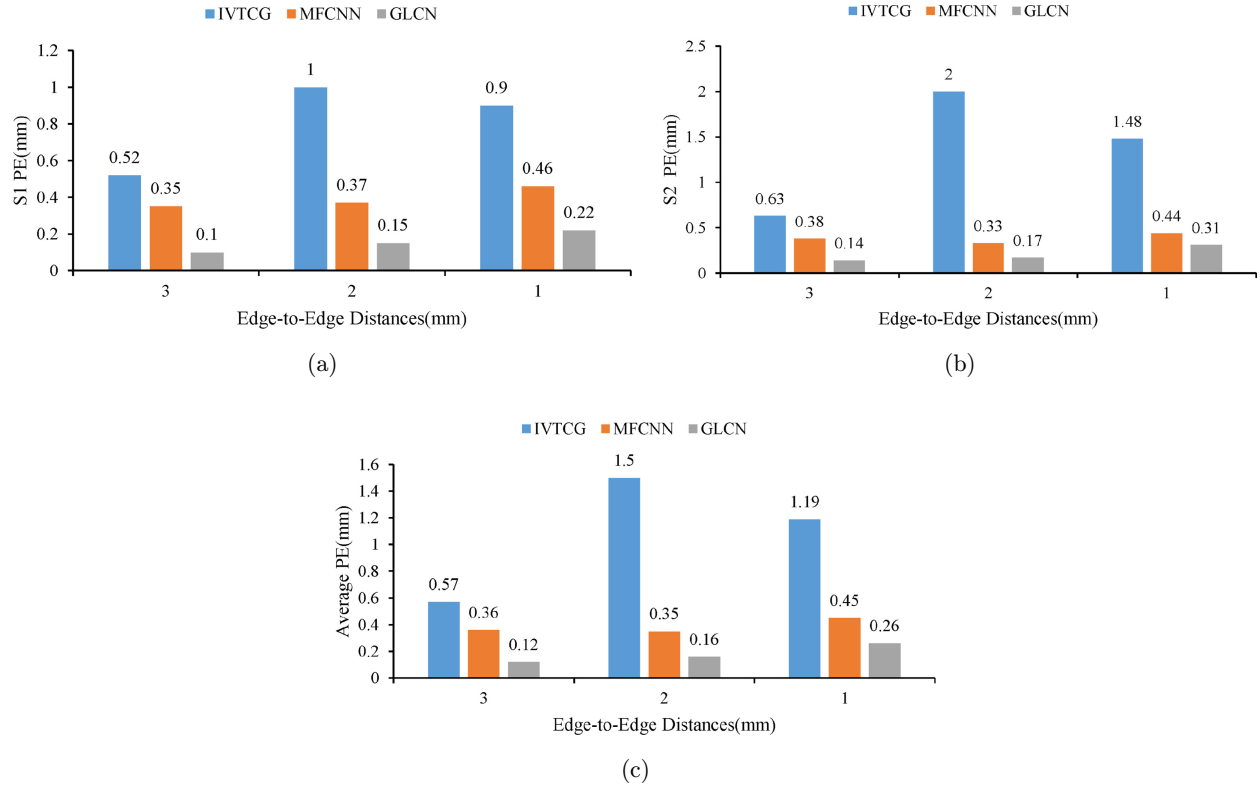


Fig. 5. Quantitative analysis was conducted on dual-source reconstruction utilizing EEDs ranging from 3 mm to 1 mm. (a) and (b) present the PE of reconstructed sources S1 and S2, respectively. (c) shows the average PE of S1 and S2.

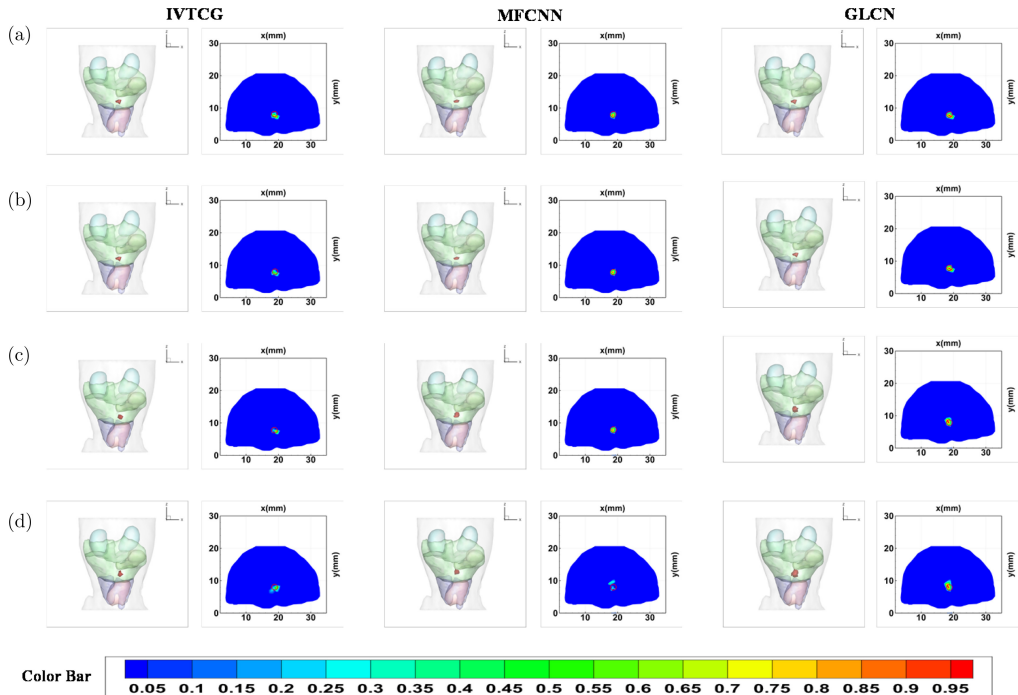


Fig. 6. OMT reconstruction results of single sources with varying noise interference levels using different methods. (a) Displays the 3D view and transverse sections of the reconstructed sources given by IVTCG, MFCNN, and GLCN, respectively. (b)–(d) demonstrate the 3D view and transverse sections of reconstructed sources with 30%, 60%, and 90% Gaussian noise using IVTCG, MFCNN, and GLCN, respectively. The red cycle represents the true source regions.

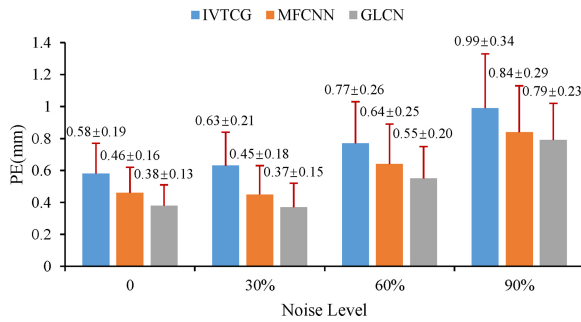


Fig. 7. Quantitative results including the mean and SD of single-source reconstruction with 0, 30%, 60%, 90% Gaussian noise given by IVTCG, MFCNN, and GLCN, respectively.

mean and SD of PE. GLCN obtains the PE of  $0.38 \pm 0.13$  mm that proves the superiority of GLCN on reconstruction accuracy for OMT. With the Gaussian noise is added to 30% level, the PE of the test sample reconstructed by three methods does not much change compared to that without noise. From 60% level Gaussian noise on, the PE of the three methods has significant increase. However, GLCN still gains the whole minimum PE ( $0.37 \pm 0.15$  mm,  $0.55 \pm 0.20$  mm,  $0.79 \pm 0.23$  mm), indicating the excellent anti-noise ability of the network.

### 3.4. Dual-source reconstruction on digital mouse simulation

Dual-source with different EEDs samples were implemented to test the reconstruction ability of GLCN. Figure 8 shows the 3D view and 2D section

images (slice at  $z = 12.5$  mm) of reconstructed source by three methods. When the EED is 3 mm, the reconstruction results of IVTCG show that the two light sources are not significant. Although the results of MFCNN and GLCN show problems such as over-spare and over-smooth, they can clearly distinguish between the two light sources. And obviously, GLCN is closer to the true source region. When the EED is 2 mm, all three methods can clearly distinguish between dual light sources. GLCN has better general overlap than the other two methods. When the EED decreases to 1 mm, adhesion occurs in the IVTCG reconstruction results. There is a significant deviation in the reconstruction position of the MFCNN dual light source. In contrast, GLCN reconstruction results are closer to the true light source area.

Quantitative comparisons demonstrated the superior performance of GLCN over the other method in localization accuracy (Fig. 9). The average PE of GLCN compared to MFCNN and IVTCG is 23.3%–59.2% and 10.9%–69.9%, respectively. In addition, when the EED of dual-source equals 1 mm, the average PE of GLCN wonderfully reached 0.1 mm. These results revealed that GLCN had a better ability for dual-source reconstruction.

### 3.5. Reconstruction time

The reconstruction time of three single-source methods for numerical cylinder and mouse

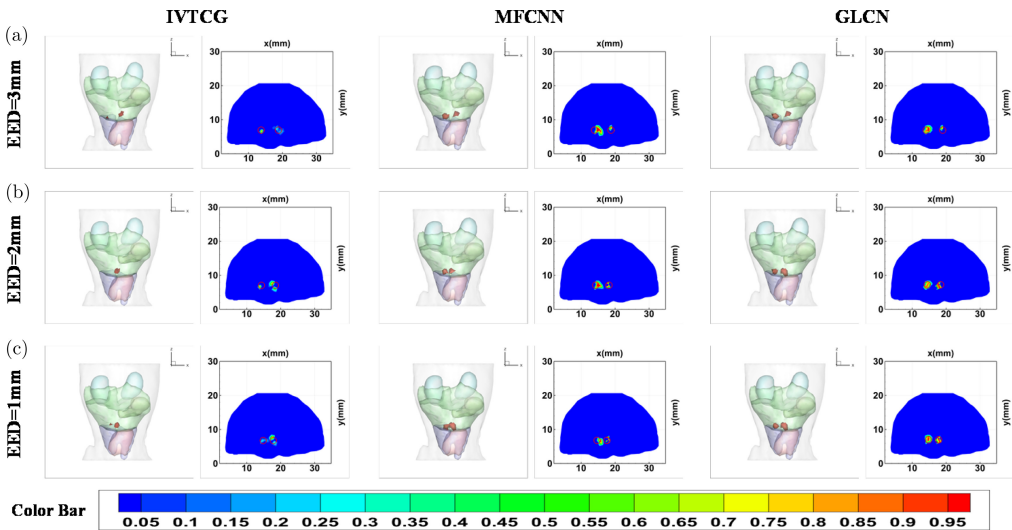


Fig. 8. OMT reconstruction results of dual-source with different EEDs. (a)–(c) depict the reconstructed sources using various methods at EEDs of 3 mm, 2 mm, and 1 mm, respectively. Both 3D rendering and 2D transverse sections were presented for comparison. The red cycle represents the true source region.

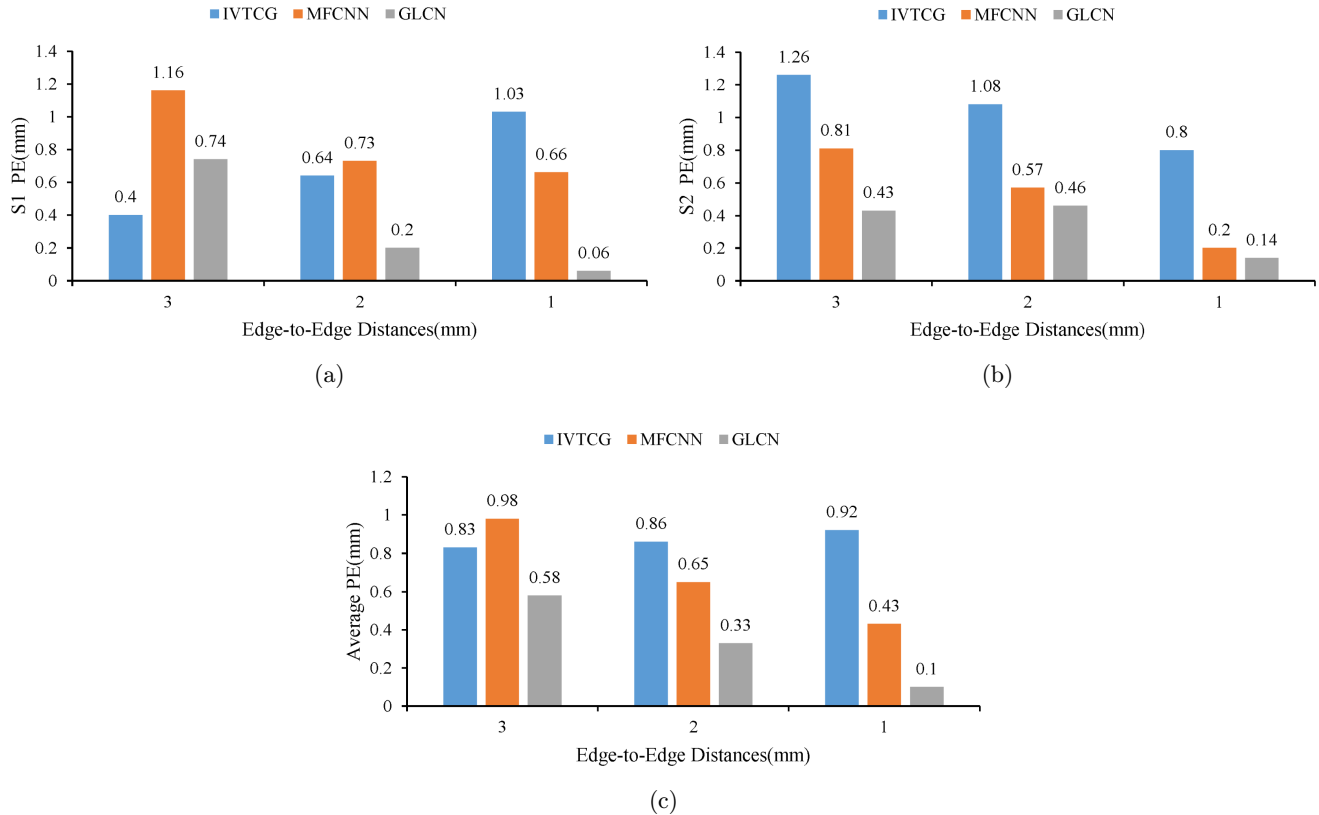


Fig. 9. Quantitative analysis was conducted on dual-source reconstruction utilizing EEDs ranging from 3 mm to 1 mm. (a) and (b) display the PE of reconstructed sources S1 and S2, respectively. (c) shows the average PE of S1 and S2.

simulations was calculated to assess the efficiency of GLCN's reconstruction (Table 1). Both model-based and data-driven methods required considerable preparation time. IVTCG method is needed to model the precise forward model and solve and optimize the inverse problem through lots of iteration steps. MFCNN and GLCN methods are needed to prepare and perform the training samples and the training process. Only the test time of MFCNN and GLCN methods and the iterative calculation time of IVTCG were collected for comparisons in this study. As shown in Table 1, the mean and SD of reconstruction time of IVTCG ( $4.79 \pm 0.20$  s) was nearly 6–7 times that of MFCNN ( $0.66 \pm 0.03$  s) and GLCN ( $0.76 \pm 0.04$  s) on cylinder simulation experiments. And on mouse simulation

experiments, the reconstruction time (mean and SD) accorded by IVTCG ( $19.59 \pm 0.41$  s) was nearly 25–30 times that of MFCNN ( $0.64 \pm 0.03$  s) and GLCN ( $0.78 \pm 0.04$  s). These results demonstrated that data-driven methods had much advantage on reconstruction efficiency than the model-based methods.

## 4. Discussion

OMT has been utilized to reconstruct the 3D distribution of targets within living animals. However, the ill-posedness of the inverse problem usually leads to inaccurate and low-robust reconstructions. Consequently, in this study, we proposed a deep learning approach (GLCN) to solve the inverse problem of OMT. This is different from the conventional methods that need to model the inverse construction process. GLCN avoids additional calculation errors and improves reconstruction efficiency. In addition, GLCN brings into gates module to implement the reconstruction process. Compared to MFCNN, this module will benefit the network to

Table 1. Time cost analysis for single source reconstruction (in units of second).

Methods	IVTCG	MFCNN	GLCN
Cylinder	$4.79 \pm 0.20$	$0.66 \pm 0.03$	$0.76 \pm 0.04$
Mouse	$19.59 \pm 0.41$	$0.64 \pm 0.03$	$0.78 \pm 0.04$

capture the crucial information of neurons that relates to the true region selectively.

Two kinds of numerical simulation experiments were carried out to evaluate the performance of GLCN from both qualitative and quantitative aspects. For single source reconstruction, GLCN obtains the best reconstruction performance with a PE down to  $0.36 \pm 0.18$  mm and  $0.38 \pm 0.13$  mm for cylinder and digital mouse-based simulation experiments, respectively. In contrast, IVTCG gains the average PE of  $0.57 \pm 0.23$  mm and  $0.58 \pm 0.19$  mm. MFCNN gains the average PE of  $0.45 \pm 0.30$  mm and  $0.46 \pm 0.16$  mm. These results proved GLCN is superior to the other two methods on accuracy and robustness (having small error fluctuation). For dual-source reconstruction, GLCN gets the lowest average PE of 0.12 mm, 0.16 mm, and 0.26 mm for EED equaling 3 mm, 2 mm, 1 mm, respectively, in cylinder-based simulation experiments. In digital mouse simulation experiments, when the EED of dual-source equals 1 mm, the average PE of GLCN wonderfully reaches 0.1 mm. These results showed that the proposed GLCN method also outperforms the other two methods in the dual-source reconstruction.

In addition, 30%, 60%, and 90% noise interference were added on the surface photon density to assess the anti-noise ability of GLCN in the single-source numerical simulation experiments. Conventional method (IVTCG) showed an obvious change when the Gaussian noise reaches 30% level, while MFCNN and GLCN showed an obvious change until noise level reaches 60%. Moreover, compared to MFCNN, GLCN robustly reconstructs the single source that is more accurate and higher overlap with overall lower PE. These results further prove the superior robustness of the GLCN.

Nevertheless, there are also some challenges. Firstly, the number of nodes used in cylinder and digital mouse models was 4626 and 13,092, respectively. The number of grids will affect the reconstruction results. We believe that finer mesh will facilitate to improve the accuracy of the reconstruction and will not affect the speed of reconstruction for deep learning methods. Secondly, GLCN, as a method of deep learning needs a pre-trained standard mesh model for reconstruction. Once the target changes, the reconstruction performance of GLCN will be greatly reduced. Thus, it is necessary for us to improve the generalization of network. Lastly, GLCN has some defects on the reconstruction

morphology. In the future, we will continue to work towards these challenging directions.

## 5. Conclusion

In summary, we proposed a GLCN to implement the accurate and robust reconstruction of OMT. The ill-posedness of OMT could be greatly reduced with the introduction of gates module. Meanwhile, gates module could improve the reconstruction accuracy and robustness of OMT. Two different kinds of numerical simulation experiments confirmed that GLCN can obtain more accurate and robust reconstruction results compared with the other two methods. This study will be a trivial exploration of OMT reconstruction. In the future, we will promote the proposed method applying to real mice-based applications.

## Acknowledgments

This study was supported by the National Natural Science Foundation of China (No. 62101439) and the Key Research and Development Program of Shaanxi (No. 2023-YBSF-289).

## Conflicts of Interest

The authors declare that there are no conflicts of interest relevant to this paper.

## ORCID

Minghua Zhao  <https://orcid.org/0000-0001-8062-2982>  
Yahui Xiao  <https://orcid.org/0009-0000-4861-363X>  
Jiaqi Zhang  <https://orcid.org/0009-0008-6903-8361>  
Xin Cao  <https://orcid.org/0000-0003-3560-6523>  
Lin Wang  <https://orcid.org/0009-0001-6949-3443>

## References

- R. John, R. Rezaeipoor, S. G. Adie, E. J. Chaney, A. L. Oldenburg, M. Marjanovic, J. P. Haldar, B. P. Sutton, S. A. Boppart, “*In vivo* magnetomotive optical molecular imaging using targeted magnetic nanoprobes,” *Proc. Natl. Acad. Sci.*, **107**(18), 8085–8090 (2010).

2. C. Chi, Y. Du, J. Ye, D. Kou, J. Qiu, J. Wang, J. Tian, X. Chen, "Intraoperative imaging-guided cancer surgery: From current fluorescence molecular imaging methods to future multi-modality imaging technology," *Theranostics*, **4**(11), 1072 (2014).
3. G. S. Mitchell, P. T. Lloyd, S. R. Cherry, "Cerenkov luminescence and pet imaging of 90y: Capabilities and limitations in small animal applications," *Phys. Med. Biol.*, **65**(6), 065006 (2020).
4. D. Fan, X. Zhang, L. Zhong, X. Liu, Y. Sun, H. Zhao, B. Jia, Z. Liu, Z. Zhu, J. Shi *et al.*, "68ga-labeled 3prgd2 for dual pet and cerenkov luminescence imaging of orthotopic human glioblastoma," *Bioconjug. Chem.*, **26**(6), 1054–1060 (2015).
5. Y. Gao, K. Wang, S. Jiang, Y. Liu, T. Ai, J. Tian, "Bioluminescence tomography based on gaussian weighted laplace prior regularization for *in vivo* morphological imaging of glioma," *IEEE Trans. Med. Imag.*, **36**(11), 2343–2354 (2017).
6. H. Liu, X. Yang, T. Song, C. Bao, L. Shi, Z. Hu, K. Wang, J. Tian, "Multispectral hybrid cerenkov luminescence tomography based on the finite element SPN method," *J. Biomed. Opt.*, **20**(8), 086007 (2015).
7. H. Guo, Y. Hou, X. He, J. Yu, J. Cheng, X. Pu, "Adaptive HP finite element method for fluorescence molecular tomography with simplified spherical harmonics approximation," *J. Innov. Opt. Health Sci.*, **7**(02), 1350057 (2014).
8. E. Ciarrocchi, N. Belcaro, "Cerenkov luminescence imaging: Physics principles and potential applications in biomedical sciences," *EJNMMI Phys.*, **4**(1), 1–31 (2017).
9. B. Zhang, W. Yin, H. Liu, X. Cao, H. Wang, "Bioluminescence tomography with structural information estimated via statistical mouse atlas registration," *Biomed. Opt. Express*, **9**(8), 3544–3558 (2018).
10. J. Yu, B. Zhang, I. I. Iordachita, J. Reyes, Z. Lu, M. V. Brock, M. S. Patterson, J. W. Wong, K. K.-H. Wang, "Systematic study of target localization for bioluminescence tomography guided radiation therapy," *Med. Phys.*, **43**(5), 2619–2629 (2016).
11. W. Cong, G. Wang, D. Kumar, Y. Liu, M. Jiang, L. V. Wang, E. A. Hoffman, G. McLennan, P. B. McCray, J. Zabner *et al.*, "Practical reconstruction method for bioluminescence tomography," *Opt. Express*, **13**(18), 6756–6771 (2005).
12. Y. Lu, A. Douraghy, H. B. Machado, D. Stout, J. Tian, H. Herschman, A. F. Chatzioannou, "Spectrally resolved bioluminescence tomography with the third-order simplified spherical harmonics approximation," *Phys. Med. Biol.*, **54**(21), 6477 (2009).
13. D. Yang, X. Chen, S. Ren, X. Qu, J. Tian, J. Liang, "Influence investigation of a void region on modeling light propagation in a heterogeneous medium," *Appl. Opt.*, **52**(3), 400–408 (2013).
14. L. Wang, X. Cao, Q. Ren, X. Chen, X. He, "Hybrid model based unified scheme for endoscopic cerenkov and radio-luminescence tomography: Simulation demonstration," *J. Appl. Phys.*, **123**(18), 184701 (2018).
15. H. Yi, D. Chen, W. Li, S. Zhu, X. Wang, J. Liang, J. Tian, "Reconstruction algorithms based on l 1-norm and l 2-norm for two imaging models of fluorescence molecular tomography: A comparative study," *J. Biomed. Opt.*, **18**(5), 056013–056013 (2013).
16. H. Guo, X. He, M. Liu, Z. Zhang, Z. Hu, J. Tian, "Weight multispectral reconstruction strategy for enhanced reconstruction accuracy and stability with cerenkov luminescence tomography," *IEEE Trans. Med. Imag.*, **36**(6), 1337–1346 (2017).
17. Y. Gao, K. Wang, Y. An, S. Jiang, H. Meng, J. Tian, "Nonmodel-based bioluminescence tomography using a machine-learning reconstruction strategy," *Optica*, **5**(11), 1451–1454 (2018).
18. S. P. Davis, S. Kumar, Y. Alexandrov, A. Bhargava, G. da Silva Xavier, G. A. Rutter, P. Frankel, E. Sahai, S. Flaxman, P. M. French *et al.*, "Convolutional neural networks for reconstruction of undersampled optical projection tomography data applied to *in vivo* imaging of zebrafish," *J. Biophoton.*, **12**(12), e201900128 (2019).
19. F. Yang, T.-A. Pham, H. Gupta, M. Unser, J. Ma, "Deep-learning projector for optical diffraction tomography," *Opt. Express*, **28**(3), 3905–3921 (2020).
20. J. Yoo, S. Sabir, D. Heo, K. H. Kim, A. Wahab, Y. Choi, S.-I. Lee, E. Y. Chae, H. H. Kim, Y. M. Bae *et al.*, "Deep learning diffuse optical tomography," *IEEE Trans. Med. Imag.*, **39**(4), 877–887 (2019).
21. Z. Zhang, M. Cai, Y. Gao, X. Shi, X. Zhang, Z. Hu, J. Tian, "A novel cerenkov luminescence tomography approach using multilayer fully connected neural network," *Phys. Med. Biol.*, **64**(24), 245010 (2019).
22. L. Guo, F. Liu, C. Cai, J. Liu, G. Zhang, "3D deep encoder-decoder network for fluorescence molecular tomography," *Opt. Lett.*, **44**(8), 1892–1895 (2019).
23. D. Li, C. Chen, J. Li, Q. Yan, "Reconstruction of fluorescence molecular tomography based on graph convolution networks," *J. Opt.*, **22**(4), 045602 (2020).
24. H. Meng, Y. Gao, X. Yang, K. Wang, J. Tian, "K-nearest neighbor based locally connected network for fast morphological reconstruction in fluorescence molecular tomography," *IEEE Trans. Med. Imag.*, **39**(10), 3019–3028 (2020).

25. C. Cao, A. Xiao, M. Cai, B. Shen, L. Guo, X. Shi, J. Tian, Z. Hu, “Excitation-based fully connected network for precise NIR-II fluorescence molecular tomography,” *Biomed. Opt. Express*, **13**(12), 6284–6299 (2022).
26. A. Graves, “Long short-term memory,” *Supervised Sequence Labelling with Recurrent Neural Networks*, Springer, Heidelberg, pp. 37–45 (2012).
27. S. Bartel, A. H. Hielscher, “Monte Carlo simulations of the diffuse backscattering Mueller matrix for highly scattering media,” *Appl. Opt.*, **39**(10), 1580–1588 (2000).
28. S. Ren, X. Chen, H. Wang, X. Qu, G. Wang, J. Liang, J. Tian, “Molecular optical simulation environment (mose): A platform for the simulation of light propagation in turbid media,” *PLoS One*, **8**(4), e61304 (2013).
29. V. H. Vu, “On the infeasibility of training neural networks with small mean-squared error,” *IEEE Trans. Inf. Theory*, **44**(7), 2892–2900 (1998).
30. D. P. Kingma, J. Ba, “Adam: A method for stochastic optimization,” arXiv:1412.6980.